APL Photonics

Demonstration of scalable microring weight bank control for large-scale photonic integrated circuits

Cite as: APL Photonics **5**, 040803 (2020); https://doi.org/10.1063/1.5144121
Submitted: 31 December 2019 . Accepted: 12 March 2020 . Published Online: 01 April 2020

Chaoran Huang, Simon Bilodeau, Thomas Ferreira de Lima, Alexander N. Tait, Philip Y. Ma, Eric C. Blow, Aashu Jha, Hsuan-Tung Peng, Bhavin J. Shastri, and Paul R. Prucnal

COLLECTIONS

Paper published as part of the special topic on Photonics and AI
Note: This article is part of the APL Photonics Special Topic on Photonics and AI.

openaccess

View Online Export Citation CrossMark

APL Photonics The Future Luminary Award
Journal Impact Factor 4.383
LEARN MORE!

© 2020 Author(s).

Demonstration of scalable microring weight bank control for large-scale photonic integrated circuits

Cite as: APL Photon. 5, 040803 (2020); doi: 10.1063/1.5144121
Submitted: 31 December 2019 • Accepted: 12 March 2020 •
Published Online: 1 April 2020

View Online Export Citation CrossMark

Chaoran Huang,[1,a)] Simon Bilodeau,[1] Thomas Ferreira de Lima,[1] Alexander N. Tait,[1,b)] Philip Y. Ma,[1] Eric C. Blow,[1] Aashu Jha,[1] Hsuan-Tung Peng,[1] Bhavin J. Shastri,[1,2] and Paul R. Prucnal[1]

AFFILIATIONS

[1]Department of Electrical Engineering, Princeton University, Princeton, New Jersey 08544, USA
[2]Department of Physics, Engineering Physics and Astronomy, Queen's University, Kingston, Ontario K7L 3N6, Canada

Note: This article is part of the APL Photonics Special Topic on Photonics and AI.
[a)]**Author to whom correspondence should be addressed:** chaoranh@princeton.edu
[b)]**Now at**: Physical Measurement Laboratory, National Institute of Standards and Technology, Boulder, CO 80305, USA.

ABSTRACT

Microring resonators (MRRs) are reconfigurable optical elements ubiquitous in photonic integrated circuits. Owing to its high sensitivity, MRR control is very challenging, especially in large-scale optical systems. In this work, we experimentally demonstrate continuous, multi-channel control of MRR weight banks using simple calibration procedures. A record-high accuracy and precision are achieved for all the controlled MRRs with negligible inter-channel crosstalk. Our approach allows accurate transmission calibration without the need for direct access to the output of the microring weight bank and without the need to lay out electrical and optical I/Os specific for calibration purpose. These features mean that our MRR control approach can be applied to large-scale photonic integrated circuits while maintaining its accuracy with manageable cost of chip area and I/O complexity.

© 2020 Author(s). All article content, except where otherwise noted, is licensed under a Creative Commons Attribution (CC BY) license (http://creativecommons.org/licenses/by/4.0/). https://doi.org/10.1063/1.5144121

I. INTRODUCTION

It has been widely recognized that photonics possesses unique advantages for information processing over electronics in terms of bandwidth and information density. These advantages have motivated extensive demonstrations of various high-performance optical functionalities in the past few decades,[1–4] despite the difficulty in achieving a sufficient scalability for optical computing. The situation has changed recently, thanks to the rapid advances in silicon photonics,[5–7] which opened up unprecedented opportunities to integrate high-performance optical functionalities and operations on a single chip to build large-scale photonic integration circuits.[8,9]

Scalability and reconfigurability are emphasized as the essential features in many large-scale information processing systems.[4,10] One of the examples is the photonic neural network in which a key functionality is to configure connection strengths between the photonic neurons.[11–15] Microring resonator (MRR) weight banks, consisting of parallel-coupled MRRs, are capable of weighting the neuron output independently over a continuous range.[16] MRR weight banks have also shown their potential as reconfigurable elements in other large-scale optical processors such as matrix multipliers for high-performance computing[17] and convolutional operators.[18]

Apart from optical information processing systems, MRR-based circuits are used extensively for applications such as wavelength-division multiplexing (WDM) filtering, waveform generation, and optical interconnects.[1,2,19] A certain degree of reconfigurability is still necessary, even in these so-called application-specific photonic integrated circuits where distinct circuits are designed to perform fixed functionalities. The reason is that some device parameters are difficult to be precisely matched as desired, owing to fabrication variance. Reconfigurable elements can be used to tune the devices to their desired states, even in the presence of fabrication variance.[10]

The high sensitivity of MRRs makes them difficult to be controlled. Prior work has demonstrated MRR control for both resonance locking and continuous transmission value configuration using feedforward and feedback approaches.[20–25] Most of the demonstrations only center on small-scale MRR systems. In this work, we demonstrate a simple and practical approach for MRR weight bank control based on the feedback control method introduced by Tait *et al.*[24] and expand its application in large-scale integrated photonic systems such as photonic neural networks. We experimentally demonstrate multi-channel MRR control using simplified procedures and achieve a record-high accuracy and precision for all the controlled channels compared to Ref. 26 by using a more accurate transmission estimation method. In addition, negligible inter-channel crosstalk is observed when we evaluate the transmission accuracy of one channel while tuning other channels over their full transmission range. The simplified procedures require only one source-meter for transmission calibration and evaluation in a weight bank, as opposed to a suite of high-speed equipment.[24,26] It also allows accurate MRR control without the need for direct access to the optical output of the microring weight bank and without the need to lay out electrical and optical I/Os specific for calibration purpose. These results imply that the demonstrated MRR control approach can be practically scaled up and applied to large-scale optical systems with maintained high accuracy and manageable cost of the chip area and I/O complexity.

II. SILICON MRR WEIGHT BANKS AND WEIGHT CONTROL SETUP

A. Device description

The silicon weight banks in this work, as shown in Fig. 1(a), are fabricated on a silicon-on-insulator (SOI) wafer with a silicon thickness of 220 nm and a buried oxide thickness of 2 μm. The weight bank consists of four MRRs coupled with two bus waveguides (500 nm width) in an add/drop configuration. The four MRRs have radii of 8.0 μm, 8.1 μm, 8.2 μm, and 8.3 μm, respectively. A slight difference is introduced in the ring radii to avoid resonance collision. The gap between the ring and the bus waveguide is 200 nm, yielding a Q factor of ~6000. For the purpose of weight control, in-ring N-doped photoconductive heaters are implemented. The N-doped heater can actuate the weight by thermally tuning the MRR resonance. At the same time, it senses the MRR transmission from the photoabsorption-induced change in the heater resistance. To implement the N-doped heater, each MRR consists of a circular waveguide etched to a 90 nm thick pedestal that hosts the phosphorous dopants. A 10 μm wide N doping section is patterned to follow the MRR, outside of which heavy N++ doping is used to make ohmic contacts. The phosphorous dopant concentrations are N: 5×10^{17} cm^{-3} and N++: 5×10^{20} cm^{-3}, as in Ref. 27. Metal vias and traces are deposited to connect the heater contacts of the MRR weight bank to electrical metal pads.

B. Experimental setup

The experimental setup is shown in Fig. 1(a). The WDM signals are obtained from four external cavity lasers (ECLs) and are multiplexed with an arrayed waveguide grating (AWG) coupler. Each signal is set to 6 dBm power before it is launched into the chip. The WDM signals are coupled into and out of the device using TE focusing grating couplers from the IN port and THRU port, respectively, with a total loss of 12 dB. An optical power meter (PM) is used for weight calibration and evaluation. The DC pads are wire-bonded to a chip carrier that is connected to Keithley 2400 source-meters. The sample is placed on a temperature-controlled stage.

The output of the WDM signals, together with the transmission spectrum of the weight bank, is measured using an optical spectrum analyzer (OSA). The result is shown in Fig. 1(c). The four signals are initially located at the short wavelength side of the MRR resonance because the thermal tuning will lead to a red-shift of the resonance. The signal wavelengths are chosen to be close to but out of the MRR resonance. The initial frequency offsets between the signals and the MRR resonance are 30 GHz, 23 GHz, 72 GHz, and 50 GHz, respectively.

III. N-DOPED PHOTOCONDUCTIVE HEATER

Optical power sensing using N-doped heaters is used to control large-scale silicon photonic circuits, as introduced by Jayatilleka *et al.*[23] The N-doped heater is formed by lightly doping the microring waveguide with donor carriers. When a current is applied to the MRR, the refractive index of the waveguide will increase, thus shifting the resonance to a longer wavelength. When there is light circulating inside the MRR, the N-doped heater will absorb a small portion of the light and creates electron–hole pairs, which, in turn, increases the conductivity of the heater. The light-induced

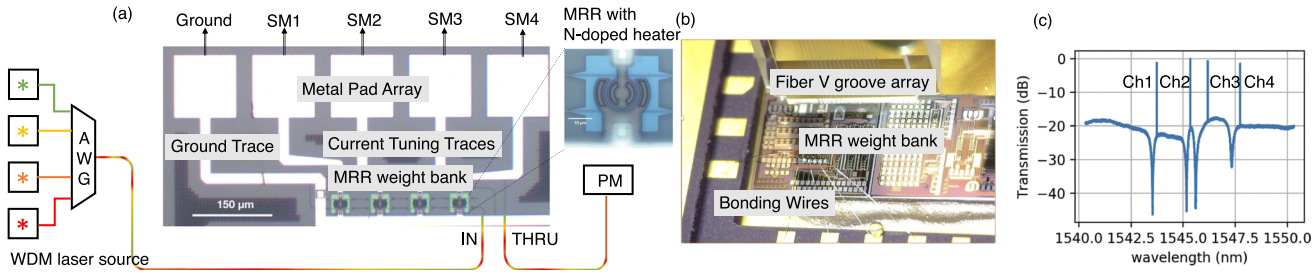

FIG. 1. (a) Schematic of the experimental setup for performing on-chip weight bank control and the optical image of the fabricated device. AWG: arrayed waveguide grating; SM: source-meter; and PM: power meter. (b) Picture of the experiment setup for optical coupling and wire bonding. (c) Optical spectrum showing the weight bank and the WDM laser sources.

© Author(s) 2020

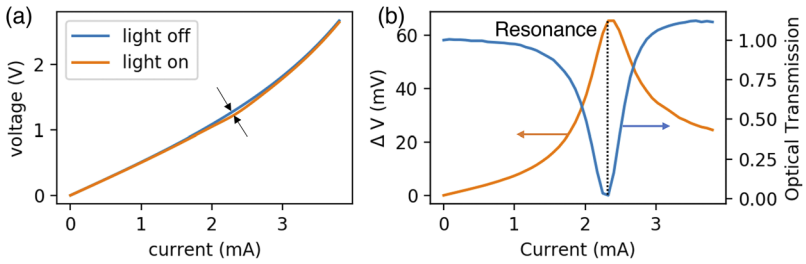

FIG. 2. (a) Electrical response of the N-doped heater against the biasing current with light on and off and (b) bias dependence of the optical transmission and ΔV evaluated from the voltage difference obtained in (a).

conductivity change can be evaluated by the voltage difference ΔV with and without the presence of light. The resonance offset determines the amount of light circulating in the MRR. Therefore, ΔV can be used to estimate the optical transmission and used as a sensor for feedback control.[24]

To illustrate the concept of the N-doped heater, we conduct thermo-electric characterization of the N-doped MRR of Ch4 as an example. The electrical response to the bias current with the laser on (orange) and off (blue) is shown in Fig. 2(a). The heater resistance is 497 Ω, and the net change in resistance against power is 40 Ω/W. We then measure the optical transmission (defined as the optical power ratio with and without applying bias current) against the bias current and plot the optical transmission together with ΔV in Fig. 2(b). As expected, the peak of ΔV (65.3 mV) and the transmission dip occur at approximately the same bias current (2.32 mA). The MRR resonance shape should be in Lorentzian shape. However, in Fig. 2(b), the curves are asymmetric around the resonance. When the heater current increases, the refractive index and the loss of the waveguide will increase. Such change will not only lead to the resonance shift but also lead to the change in the extinction ratio, Q factor, and resonance shape. Due to these changes, we observe different degrees of symmetry between the right edge and the left edge of the resonance. For the same reason, the peaks of blue and orange curves are slightly offset. More specifically, around the resonance peak, even when the transmission is slightly tuned by different heater biases, the power inside the MRR (which corresponds to photoresponse ΔV) may not change because the Q factor at different heater biases can be slightly different. This can be the reason why there is a small pedestal at ΔV and why the peak of ΔV and transmission T are slightly offset.

IV. MULTI-CHANNEL CALIBRATION PROCEDURES

This section describes the calibration procedure in steps including common parasitic resistance calibration, baseline calibration, photoresponse calibration, and transmission edge calibration. A control rule is enabled after these steps.

A. Common parasitic resistance calibration

The MRRs share a common ground trace (Fig. 1) that causes a common parasitic resistance between each MRR. Therefore, in multi-channel calibration, the measured voltage is a combination of the actual voltage on the heater and the voltage caused by the common parasitic resistance (i.e., $V_{measured} = V_{heater} + V_{common}$). Since the estimation of the optical transmission relies on the accurate measurement of V_{heater}, the common parasitic resistance needs to be first characterized and extracted. The common parasitic resistance forms an N × N resistance network, where N is the channel number. The element $R_{common,\,j,i}$ is characterized by measuring the voltage on the heater j ($V_{measure,j}$) while sourcing a small current I_{set} (I_{set} = 10 μA in the experiment) only on the heater i. Then, $R_{common,\,j,i} = V_{measure,j}/I_{set}$. After this step, the actual heater voltages can be derived from the measured voltages by applying the R_{common} matrix to the known vector of currents.

B. Baseline calibration

Baseline calibration is to assess the electric and thermo-electric properties of the N-doped heater, while the light is off and, as a result, provides a baseline for the photoresponse characterization. The current is swept, and the voltage is measured on each heater sequentially. After sweeping, the I–V function is obtained, together with the ambient resistance and the thermo-electric coefficient of each heater by least squares polynomial fit.

C. Photoresponse calibration

1. Photoresponse peak search

This step is to determine the maximum photovoltage, ΔV_{max}, which indicates the optical resonance, and the corresponding current I_{res} and electrical power P_{res} that are applied at the resonance. A Nelder–Mead search is used to converge on the peak photoresponse occurring at the resonance.[24,28] When performing the photoresponse peak search, we turn on all four signals. The peak search is conducted on each channel twice: first, a rough search is conducted with an error tolerance of 10% sequentially on each channel; second a fine search is conducted with an error tolerance of 1% for individual channels, while the other channels are tuned to resonance by applying the estimated P_{res} obtained during the first search; and finally, the P_{res} and ΔV_{max} are updated to the values obtained from the second search. Such a two-time search can avoid any channel being influenced by large tuning of the other channels due to thermal crosstalk. We now define a term *normalized photoresponse* as $\hat{D}$. Both the blue side and the red side of the MRR resonance line shape can be used for weighting. In our experiment, we only use the blue side because it requires a lower tuning power. In this case, $\hat{D}$ is calculated using $\hat{D} = 1 - (\Delta V/\Delta V_{max})^2$.[24] The value of $\hat{D}$ is used to estimate the actual transmission value (or weight) D.

2. Photoresponse HWHM search

This step involves looking for the photoresponse, that is, half of the peak photoresponse (i.e., $\hat{D}_{max}/2$) and the corresponding current I_{HWHM} and electrical power P_{HWHM} using the binary search method. All four signals are turned on in this step. During binary

© Author(s) 2020

search, if the photoresponse is larger than $\hat{D}_{max}/2$, the applied electrical power is reduced; otherwise, the electrical power is increased. In every iteration, the magnitude of the power step is halved until the search converges, resulting in a half-width at half-maximum power P_{HWHM}. Like the photoresponse peak search, the HWHM search is also repeated twice on each channel to mitigate the effect of thermal crosstalk. Now, we define a parameter for the normalized electrical power, δ, as

$$\delta = \frac{P_{res} - P}{P_{HWHM}}. \quad (1)$$

When $\delta = 1$, the optical transmission is half of the maximum.

D. Transmission edge calibration

In this step, we calibrate the relation between the actual optical transmission D and the normalized electrical power δ. In the single channel case, we observed from our previous work that the actual transmission D approximately equals to $\hat{D}$, which indicates that D is linear to δ.[24] However, such an estimation cannot be generally applied to every device due to parameter (e.g., resistance, photoresponsivity, and self-heating) variance. In addition, such an estimation is not accurate in the multi-channel case, especially when the transmission spectra of different MRRs are slightly overlapped, as shown in Fig. 1(c). Device variance and spectral overlapping are difficult to be controlled due to fabrication variance. Figure 3 plots the relation between the estimated transmission $\hat{D}$ and the measured transmission D (blue curve), compared with the ideal estimation shown with the black dashed line. The relationship is nonlinear, indicating that the transmission edge must be calibrated for accurate control.

In our previous work,[24] the transmission edge calibration is conducted simultaneously on two channels by using scope-based decomposition of the 2 × 2 weight matrix. This approach requires expensive external equipment for signal generation and detection, such as pattern generator, photodetector (PD), and sampling oscilloscope. In addition, scaling this approach to a large number of channels is challenging. The accuracy of this approach depends on the dynamic range of the photodetectors and the oscilloscope, as well as the sampling precision of the oscilloscope. Therefore, as the channel number increases, the weight decomposition accuracy will decrease. For example, as the channel number increases, the PD will saturate, which, in turn, reduces the accuracy of weight decomposition. Here, we adopt a simplified edge transmission calibration using only an optical power meter. The calibration is conducted on the 4 channels sequentially: only one laser that is paired with the evaluated MRR is turned on, while other lasers are turned off. At the same time, the MRRs that are not under evaluation are tuned to resonance by applying the calibrated P_{res}. A set of binary searches is performed to track the photoresponse to 10 values over the range 0–1, and the real transmission is measured using the optical power meter. After this step, we obtain the function g between $\hat{D}$ and D and can update the photoresponse with the calibrated optical transmission $[\hat{D} \rightarrow g(\hat{D})]$. This procedure is valid if the weighting signals do not share the same optical amplifier. Eventually, a control rule $\delta \rightarrow \hat{D}$ for weight control is developed.

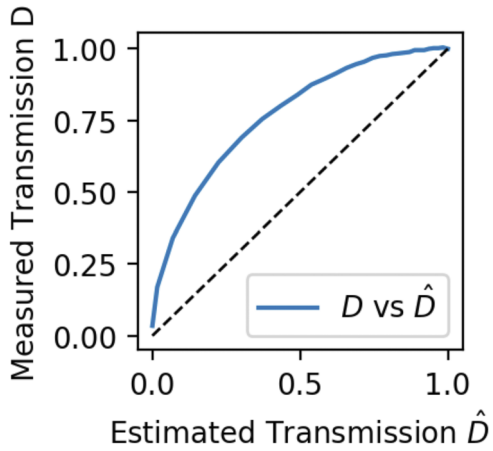

FIG. 3. Relation between the estimated transmission $\hat{D}$ and the measured transmission D (blue curve), compared with ideal estimation (black dashed line).

V. CONTROL PROCEDURE AND RESULTS

The control rule $\delta \rightarrow \hat{D}$ developed in the calibration stage is applied for weight control. The controller converts the command weight to an applied current using binary search based on the control rule. If the sensed photoresponse $\hat{D}$ is smaller than the command weight, the current increases to push the resonance closer to the laser wavelength. If $\hat{D}$ is larger than the command weight, the current decreases to increase the offset between the resonance and the laser wavelength. In every iteration, the magnitude of the power step is halved until the search converges, and as a result, a desired weight is actuated.

We evaluate the performance of the developed control rule on the four channels. The evaluator generates a four-dimension command weight: eight weight values are actuated on the channel under evaluation, while three values are actuated on the other three channels. The weight values are evenly distributed over a range of (0, 1). The evaluator then measures the actual weight using the optical power meter and calculates the difference between the measured weight and the command weight. The evaluation is performed as the other three channels are jointly swept across their range of operation to study the crosstalk in the multichannel scenario. The performance is quantified in terms of accuracy and precision, as defined in Refs. 24 and 25. Here, accuracy is the mean deviation from the command weights, i.e., $\sigma_{accu} = \|\bar{\mu} - \hat{\mu}\|$, and precision is the non-repeatable standard deviation around this mean, i.e., $\sqrt{\langle(\mu - \bar{\mu})^2\rangle}$. μ is the measured weight, $\bar{\mu}$ is the mean over the measured weight, and $\hat{\mu}$ is the command weight.

The four-channel weight control results are shown in Fig. 4. Figure 4(a) shows the measured weight as a function of the command weight for each channel under evaluation. The ideal target weights are also displayed (black dashed line). The other three channels are jointly actuated with a weight in the list [0, 0.5, 1]. Figure 4(b) shows the offset between the measured weight and the command weight for a given channel. The black crosses denote the mean offset from the ideal weight. The black vertical lines show the standard deviation of the measured weight. The offset values are used to evaluate the accuracy and precision, and the results are

© Author(s) 2020

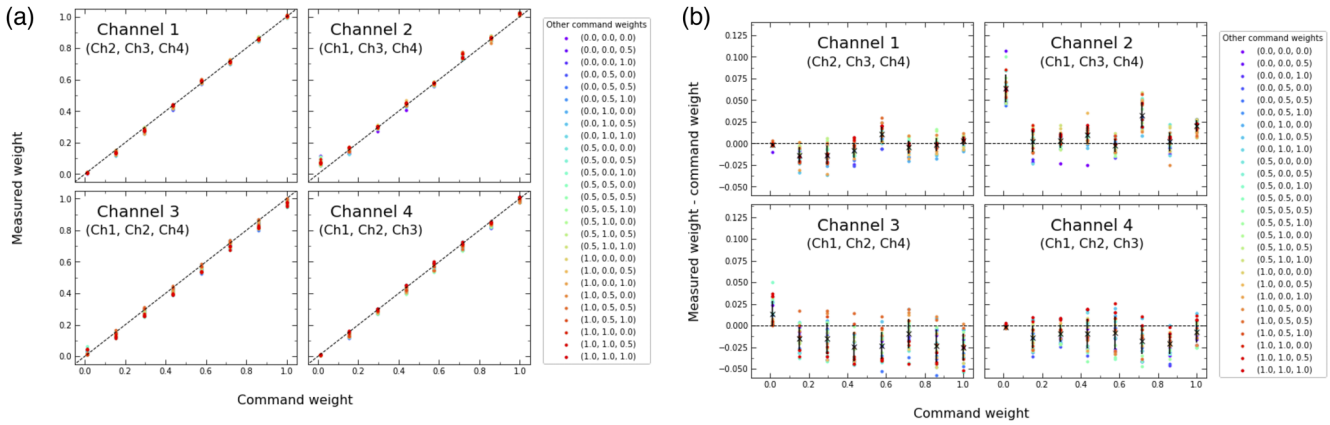

FIG. 4. (a) Measured weights and (b) offset between a given measured weight and command weight as a function of command weights for a given channel. For each datapoint, the tuples in the legend contain the command weight values for the other channels in the order displayed below the plot label. The dashed lines in (a) represent the ideal target weights. The black crosses in (b) denote the mean offset from the ideal weight (reproducible offset). The black vertical lines in (b) show the standard deviation of the measured weight (non-reproducible offset).

summarized in Table I. A record-high accuracy and precision are achieved in all four channels, to the best of our knowledge.[26] The demonstrated accuracy significantly outperforms the digital weight resolution (5 bits) used in the TrueNorth architecture.[29]

To study the crosstalk among the four channels, the mean deviation from the eight command weights on Ch4 is plotted against the command weights on the other three channels. The result is shown in Fig. 5. The potential crosstalk in this work includes contributions of both electrical and thermal crosstalk. Electrical crosstalk is mainly caused by the common parasitic resistance that has been corrected in the calibration procedure described in Sec. IV A. Thermal crosstalk occurs as local heat leaks to the surroundings, resulting in the resonance change in the neighboring channels. Thermal crosstalk is most severe when all the channels are tuned to resonance [i.e., command weight is (0, 0, 0)] since the largest currents need to be applied. However, as shown in Fig. 5, the measured error at command weight (0, 0, 0) is comparable to that at command weight (1, 1, 1) (no currents are applied). This result implies that the thermal crosstalk becomes negligible because of the two-time calibration of the resonance peak and HWHM. In addition, several general approaches can be incorporated to further reduce the thermal crosstalk even when a large heating current is applied. Examples include Ref. 30 in which thermal eigenmode decomposition is used to decouple the thermally coupled system and Ref. 31 in which thermal insulation trenches are added to prevent unwanted leakage of heat. The third type of crosstalk in the MRR weight bank comes from the spectral overlap. The spectral overlap occurs when the transmission resonance of one channel overlaps with that of other channels. In this case, the MRR weight bank cannot be broken into N independent models and our weight calibration will not be applied. In our current design, the MRR channels are far apart to avoid such crosstalk.

TABLE I. Accuracy and precision measurement.

Channel	1	2	3	4
Accuracy (bits)	7.2	5.5	6.0	6.6
Precision (bits)	7.2	6.8	6.2	6.5

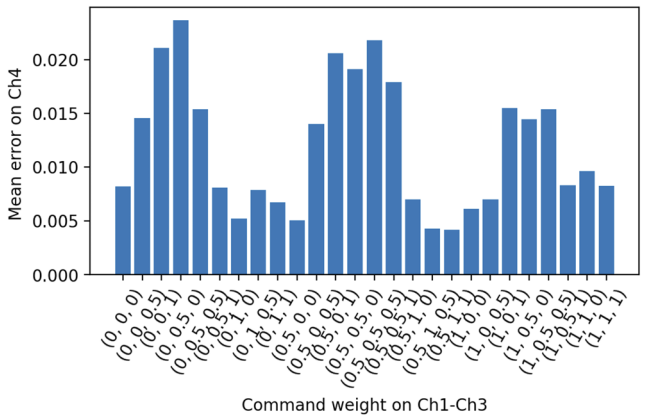

FIG. 5. Mean deviation over the eight command weights against the command weights on the other three channels.

VI. DISCUSSION

A. Dynamic range of input optical power

The accuracy of our weight control algorithm relies on the precise measurement of photovoltage (ΔV). The high-precision sourcemeter (Keithley 2400) has a measurement resolution of 2 μV and an accuracy of 0.012% under the operation range of 2 V. We characterize the weight control accuracy as a function optical input power on Ch4 as an example. As shown in Fig. 6, when the input optical

© Author(s) 2020

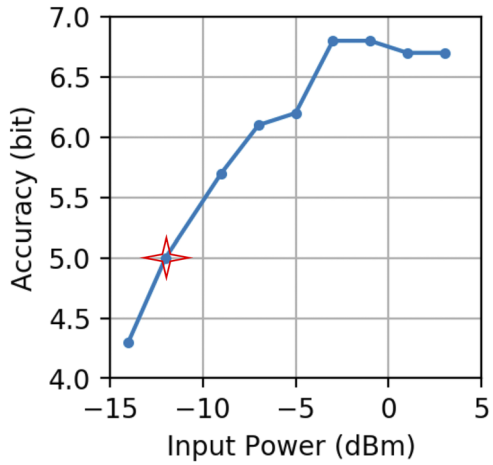

FIG. 6. Weight control accuracy against the input power. The input power is the optical power before the weight bank, calculated by subtracting the optical coupling loss from the optical power sent to the V groove array.

power is less than −3 dBm, weight control accuracy increases with the optical input power. The achieved control accuracy can meet the weight resolution used in neuromorphic electronics (5 bits) when the input optical power is −12 dBm. At this point, the measured photovoltage peak is 150 μV. Weight control accuracy starts to saturate at an input power of −3 dBm, implying that the measurement resolution and accuracy of the source-meter are no longer the limiting factor for weight control. Further increasing the optical power beyond 0 dBm can potentially trigger optical nonlinearity in silicon and lead to optical bistability featuring as a transmission hysteresis loop. The bistable optical transmission is much more challenging to be characterized in the transmission edge calibration step, compared to the linear case. This is a potential reason why a slight accuracy degradation is observed when the input power is larger than 0 dBm.

The results shown in Fig. 6 are only applied to our device under test. The input power dynamic range should depend on the Q factor of MRRs because the Q factor is approximately proportional to the resonant build-up factor. With the same input power, a higher Q factor leads to a larger photoresponse. The MRRs with a high Q factor can reduce the minimum optical power required for accurate transmission control. However, a high Q factor also leads to stronger optical nonlinear effects. Therefore, MRR with a high Q factor will allow a lower maximum power input.[32]

B. Dynamic range of frequency offset

Due to the increasing demand in optical communications, WDM lasers matching with an ITU grid have become standard and cost-effective light sources. WDM lasers can span the whole C or L band; however, they only contain discrete frequencies matching with the ITU grid with 100 GHz spacing. The initial frequency of the MRR resonance is difficult to be precisely controlled, owing to fabrication variance. Here, we characterize whether our weight control rule can be operated with any MRR resonance frequency if WDM lasers are used as light sources. We measure the weight control accuracy against the initial frequency offsets between the laser and the MRR resonance on Ch4. Five frequency offset values are evaluated over a range of over 100 GHz. As shown in Fig. 7, the weight accuracy at different initial frequency offsets is approximately the same (6.5 bits), indicating that cost-effective WDM lasers can serve as the light source, regardless of the initial frequency of the MRR resonances. In choosing the laser frequency from the available WDM channels, it is suggested (but not required) to place the laser as close to the resonance edge as possible. This can avoid sourcing the excessive tuning current, thus reducing the heat-induced waveguide loss and thermal crosstalk.

C. Weight control in photonic neural network

Prior work on continuous transmission control in silicon photonics requires direct access to the weight bank output. For example, in Ref. 24, a high-speed electrical output was needed for transmission calibration. In Ref. 16, calibration is performed on the optical spectra of the weight banks. However, in large-scale photonic systems, such as photonic neural networks, the weight bank output is not directly accessible, as shown in Fig. 8.[33] In photonic neural networks, a MRR weight bank provides the key functionality to configure connection strengths in the analog WDM network. The weight on each MRR is determined by how much of a given WDM channel is split between two ports of a balanced photodetector (BPD), as shown in Fig. 8(b). The detected signal drives an electro-optical (EO) modulator of which the nonlinear transfer function serves as the activation function of a neuron. In such a design, both optical output and electrical output of the weight banks are not directly available for calibration and measurement.

As opposed to Refs. 16 and 24, in our work, only the DC power of the weight bank output is needed for transmission calibration, which can be easily performed by measuring the DC photocurrent generated in the BPDs. As shown in Fig. 8(b), V+ and V− are applied across the PN junctions of the BPD for PD biasing using two source-meters. In+ and In− are the complementary response of the

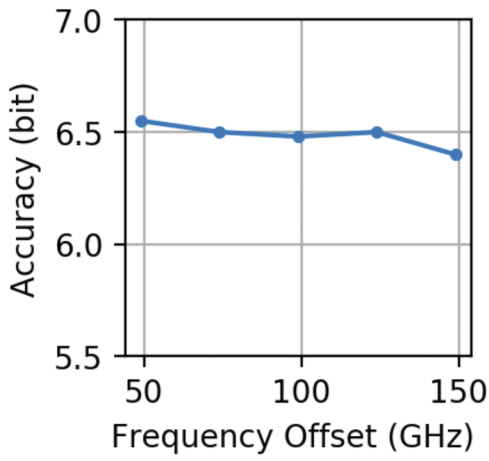

FIG. 7. Weight control accuracy against the frequency offset between the MRR and the laser.

© Author(s) 2020

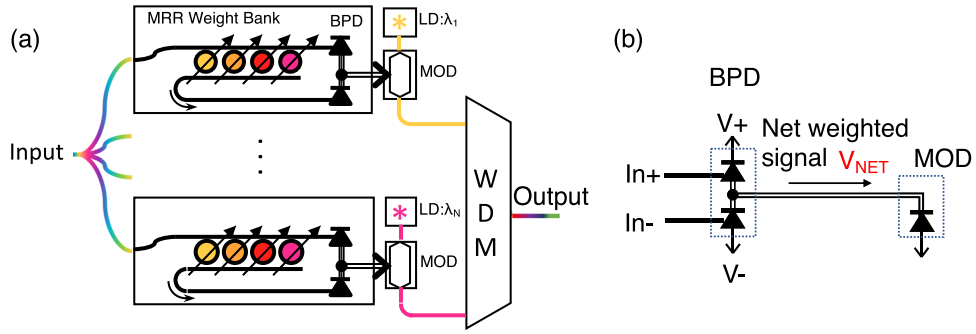

FIG. 8. (a) Schematic of the photonic neural network: An array of source laser output distinct wavelengths are multiplexed (WDM) in a single waveguide. Independent weighting functions are realized by tunable spectral filters at the input of each unit using weight banks. The total optical power of each spectrally weighted signal is detected by using a balanced photodetector (BPD), yielding the sum of the input channels. The electronic signal is transduced to an optical signal with an optical modulator. Reproduced with permission from Tait *et al.*, Sci. Rep. **7**, 7430 (2017). Copyright 2017 Springer Nature. (b) Schematic of the photonic neuron circuit. In+ and In− are the photonic output of a weight bank. Positive and negative weights are the net response of both PDs in the BPD. V+ and V− are supply powers of the BPD. V_{NET} is the sum of weighted signals and is measured for transmission calibration. Only one SM is needed for V_{NET} measurement, in addition to four SMs for weights.

weight bank. The positive and negative weights are a net response of both PDs in the BPD. Therefore, the transmission calibration can be performed by measuring V_{NET} using a source-meter connected to the BPD. With such a configuration, one can easily calibrate the weight bank, especially its transmission edge, and evaluate the control accuracy, without laying out additional optical or electrical I/O only for calibration purpose.

VII. CONCLUSION

In this work, we experimentally demonstrate continuous, multi-channel control of a microring weight bank using a simple and accurate control procedure. The experimental demonstration of the four-channel weight bank control achieves a record-high accuracy and precision up to 7 bits. Negligible inter-channel crosstalk is observed when we evaluate the transmission accuracy of one channel while tuning other channels over their full transmission range. Furthermore, we characterize the dynamic range of our MRR control approach in terms of input optical power and frequency. A minimum input power of only −12 dBm is sufficient to achieve the weight resolution (5 bit) used in neuromorphic electronics. Similar accuracy is achieved for different initial frequency offsets covering an WDM channel spacing (100 GHz), indicating that cost-effective WDM lasers can serve as the light source, regardless of the initial frequency of the MRR resonances. Our approach allows accurate transmission calibration without the need for direct access to the output of the microring weight bank and without the need to lay out electrical and optical I/Os specific for calibration purpose. The results suggest that our MRR control scheme can scale to large networks while maintaining high accuracy with manageable cost. Currently, our calibration procedures require that the MRR channels have no spectral overlap such that the MRR weight bank can be broken into N independent channels. The estimated capacity of MRRs is ~60 wavelength channels with 0.8 nm minimum wavelength spacing.[32] Further work could develop control procedures that can jointly calibrate all the channels in the MRR weight bank to combat the weight interdependency caused by spectral overlapping and increase the channel density. Further work could also implement other types of MRRs for weight control to increase the control accuracy and efficiency.[34,35]

ACKNOWLEDGMENTS

This research was supported by the Office of Naval Research (ONR) (Grant No. N00014-18-1-2297) and the Defense Advanced Research Projects Agency (Grant No. HR00111990049). Fabrication support was provided by the Natural Sciences and Engineering Research Council of Canada (NSERC) Silicon Electronic-Photonic Integrated Circuits (SiEPIC) Program, and the Canadian Microelectronics Corporation (CMC). We would also like to thank Dr. Shinsuke Fujisawa, Dr. Yue Tian, and Dr. Ting Wang from NEC Laboratories America, Inc., for providing the equipment and thoughtful discussions.

REFERENCES

[1] J. Wang, H. Shen, L. Fan, R. Wu, B. Niu, L. T. Varghese, Y. Xuan, D. E. Leaird, X. Wang, F. Gan *et al.*, "Reconfigurable radio-frequency arbitrary waveforms synthesized in a silicon photonic chip," Nat. Commun. **6**, 5957 (2015).
[2] L. Zhou and A. W. Poon, "Electrically reconfigurable silicon microring resonator-based filter with waveguide-coupled feedback," Opt. Express **15**, 9194–9204 (2007).
[3] C. Huang, T. F. de Lima, A. Jha, S. Abbaslou, A. N. Tait, B. J. Shastri, and P. R. Prucnal, "Programmable silicon photonic optical thresholder," IEEE Photonics Technol. Lett. **31**, 1834–1837 (2019).
[4] W. Liu, M. Li, R. S. Guzzon, E. J. Norberg, J. S. Parker, M. Lu, L. A. Coldren, and J. Yao, "A fully reconfigurable photonic integrated signal processor," Nat. Photonics **10**, 190 (2016).
[5] L. Chrostowski, H. Shoman, M. Hammood, H. Yun, J. Jhoja, E. Luan, S. Lin, A. Mistry, D. Witt, N. A. Jaeger *et al.*, "Silicon photonic circuit design using rapid prototyping foundry process design kits," IEEE J. Sel. Top. Quantum Electron. **25**, 1–26 (2019).
[6] D. Thomson, A. Zilkie, J. E. Bowers, T. Komljenovic, G. T. Reed, L. Vivien, D. Marris-Morini, E. Cassan, L. Virot, J.-M. Fédéli *et al.*, "Roadmap on silicon photonics," J. Opt. **18**, 073003 (2016).
[7] A. E.-J. Lim, J. Song, Q. Fang, C. Li, X. Tu, N. Duan, K. K. Chen, R. P.-C. Tern, and T.-Y. Liow, "Review of silicon photonics foundry efforts," IEEE J. Sel. Top. Quantum Electron. **20**, 405–416 (2013).

© Author(s) 2020

[8]N. C. Harris, D. Bunandar, M. Pant, G. R. Steinbrecher, J. Mower, M. Prabhu, T. Baehr-Jones, M. Hochberg, and D. Englund, "Large-scale quantum photonic circuits in silicon," Nanophotonics **5**, 456–468 (2016).
[9]J. Sun, E. Timurdogan, A. Yaacobi, E. S. Hosseini, and M. R. Watts, "Large-scale nanophotonic phased array," Nature **493**, 195 (2013).
[10]D. Pérez, I. Gasulla, L. Crudgington, D. J. Thomson, A. Z. Khokhar, K. Li, W. Cao, G. Z. Mashanovich, and J. Capmany, "Multipurpose silicon photonics signal processor core," Nat. Commun. **8**, 636 (2017).
[11]P. R. Prucnal and B. J. Shastri, *Neuromorphic Photonics* (CRC Press, 2017).
[12]A. N. Tait, T. F. de Lima, M. A. Nahmias, H. B. Miller, H.-T. Peng, B. J. Shastri, and P. R. Prucnal, "Silicon photonic modulator neuron," Phys. Rev. Appl. **11**, 064043 (2019).
[13]H.-T. Peng, M. A. Nahmias, T. F. De Lima, A. N. Tait, and B. J. Shastri, "Neuromorphic photonic integrated circuits," IEEE J. Sel. Top. Quantum Electron. **24**, 1–15 (2018).
[14]I. A. Williamson, T. W. Hughes, M. Minkov, B. Bartlett, S. Pai, and S. Fan, "Reprogrammable electro-optic nonlinear activation functions for optical neural networks," arXiv:1903.04579 (2019).
[15]Y. Shen, N. C. Harris, S. Skirlo, M. Prabhu, T. Baehr-Jones, M. Hochberg, X. Sun, S. Zhao, H. Larochelle, D. Englund *et al.*, "Deep learning with coherent nanophotonic circuits," Nat. Photonics **11**, 441 (2017).
[16]A. N. Tait, A. X. Wu, T. F. De Lima, E. Zhou, B. J. Shastri, M. A. Nahmias, and P. R. Prucnal, "Microring weight banks," IEEE J. Sel. Top. Quantum Electron. **22**, 312–325 (2016).
[17]M. A. Nahmias, T. F. De Lima, A. N. Tait, H.-T. Peng, B. J. Shastri, and P. R. Prucnal, "Photonic multiply-accumulate operations for neural networks," IEEE J. Sel. Top. Quantum Electron. **26**, 1–18 (2019).
[18]V. Bangari, B. A. Marquez, H. Miller, A. N. Tait, M. A. Nahmias, T. F. De Lima, H.-T. Peng, P. R. Prucnal, and B. J. Shastri, "Digital electronics and analog photonics for convolutional neural networks (DEAP-CNNs)," IEEE J. Sel. Top. Quantum Electron. **26**, 1–13 (2019).
[19]X. Wu, C. Huang, K. Xu, C. Shu, and H. K. Tsang, "Mode-division multiplexing for silicon photonic network-on-chip," J. Lightwave Technol. **35**, 3223–3228 (2017).
[20]Y. Li and A. W. Poon, "Active resonance wavelength stabilization for silicon microring resonators with an in-resonator defect-state-absorption-based photodetector," Opt. Express **23**, 360–372 (2015).
[21]J. C. Mak, W. D. Sacher, T. Xue, J. C. Mikkelsen, Z. Yong, and J. K. Poon, "Automatic resonance alignment of high-order microring filters," IEEE J. Quantum Electron. **51**, 1–11 (2015).
[22]P. Dong, R. Gatdula, K. Kim, J. H. Sinsky, A. Melikyan, Y.-K. Chen, G. De Valicourt, and J. Lee, "Simultaneous wavelength locking of microring modulator array with a single monitoring signal," Opt. Express **25**, 16040–16046 (2017).
[23]H. Jayatilleka, K. Murray, M. Á. Guillén-Torres, M. Caverley, R. Hu, N. A. F. Jaeger, L. Chrostowski, and S. Shekhar, "Wavelength tuning and stabilization of microring-based filters using silicon in-resonator photoconductive heaters," Opt. Express **23**, 25084–25097 (2015).
[24]A. N. Tait, H. Jayatilleka, T. F. De Lima, P. Y. Ma, M. A. Nahmias, B. J. Shastri, S. Shekhar, L. Chrostowski, and P. R. Prucnal, "Feedback control for microring weight banks," Opt. Express **26**, 26422–26443 (2018).
[25]A. N. Tait, T. F. De Lima, M. A. Nahmias, B. J. Shastri, and P. R. Prucnal, "Multi-channel control for microring weight banks," Opt. Express **24**, 8895–8906 (2016).
[26]P. Y. Ma, A. N. Tait, T. F. de Lima, S. Abbaslou, B. J. Shastri, and P. R. Prucnal, "Photonic principal component analysis using an on-chip microring weight bank," Opt. Express **27**, 18329–18342 (2019).
[27]T. Baehr-Jones, R. Ding, A. Ayazi, T. Pinguet, M. Streshinsky, N. Harris, J. Li, L. He, M. Gould, Y. Zhang *et al.*, "A 25 Gb/s silicon photonics platform," arXiv:1203.0767 (2012).
[28]J. A. Nelder and R. Mead, "A simplex method for function minimization," Comput. J. **7**, 308–313 (1965).
[29]F. Akopyan, J. Sawada, A. Cassidy, R. Alvarez-Icaza, J. Arthur, P. Merolla, N. Imam, Y. Nakamura, P. Datta, G.-J. Nam *et al.*, "Truenorth: Design and tool flow of a 65 mW 1 million neuron programmable neurosynaptic chip," IEEE Trans. Comput.-Aided Des. Integr. Circuits Syst. **34**, 1537–1557 (2015).
[30]M. Milanizadeh, D. Aguiar, A. Melloni, and F. Morichetti, "Canceling thermal cross-talk effects in photonic integrated circuits," J. Lightwave Technol. **37**, 1325–1332 (2019).
[31]A. Masood, M. Pantouvaki, G. Lepage, P. Verheyen, J. Van Campenhout, P. Absil, D. Van Thourhout, and W. Bogaerts, "Comparison of heater architectures for thermal control of silicon photonic circuits," in *10th International Conference on Group IV Photonics* (IEEE, 2013), pp. 83–84.
[32]K. Preston, N. Sherwood-Droz, J. S. Levy, and M. Lipson, "Performance guidelines for WDM interconnects based on silicon microring resonators," in *CLEO: 2011-Laser Science to Photonic Applications* (IEEE, 2011), pp. 1–2.
[33]A. N. Tait, T. F. De Lima, E. Zhou, A. X. Wu, M. A. Nahmias, B. J. Shastri, and P. R. Prucnal, "Neuromorphic photonic networks using silicon photonic weight banks," Sci. Rep. **7**, 7430 (2017).
[34]L. Gu, L. Fang, H. Fang, J. Li, J. Zheng, J. Zhao, Q. Zhao, and X. Gan, "Fano resonance lineshapes in a waveguide-microring structure enabled by an air-hole," APL Photonics **5**, 016108 (2020).
[35]A. N. Tait, A. X. Wu, T. F. De Lima, M. A. Nahmias, B. J. Shastri, and P. R. Prucnal, "Two-pole microring weight banks," Opt. Lett. **43**, 2276–2279 (2018).

© Author(s) 2020